

In-Situ and Real-Time Analysis of the Formation of Strains and Microstructure Defects during Solidification of Al-3.5 Wt Pct Ni Alloys

G. REINHART, A. BUFFET, H. NGUYEN-THI, B. BILLIA, H. JUNG,
N. MANGELINCK-NOËL, N. BERGEON, T. SCHENK, J. HÄRTWIG,
and J. BARUCHEL

Alloy solidification was investigated *in situ* and real time by using a unique experimental setup developed at the European Synchrotron Radiation Facility (ESRF) combining both synchrotron X-ray radiography and topography. Although synchrotron X-ray radiography enables the investigation of the solid-liquid interface of metallic alloys, white-beam synchrotron X-ray topography enables the investigation of the formation of strains and defects formation in the growing solid microstructure. In this article, we present results obtained during directional solidification experiments performed with Al-3.5 wt pct Ni samples. First, the initial state after thermal stabilization is characterized. Next, the interface morphological instability and the transition to the columnar growth regime are thoroughly investigated. Topography observation shows that several parts of each dendrite become disoriented while the microstructure is developing. Disorientations are quantified and the aluminum yield stress at the melting point is estimated from the bending of secondary arms. Last, coupled growth of eutectic and dendrites settles with the formation of the eutectic phase. The eutectic grains grow strained and the dendrites concomitantly undergo additional stress.

DOI: 10.1007/s11661-007-9449-2
© The Author(s) 2008

I. INTRODUCTION

STRAINS occurring during the processing of metallic alloys are critical phenomena which often determine the final quality of solidified products. Yet, their importance remains unclear during the solidification step because of the difficulty of performing observations of the microstructure formation in such opaque systems, which also have a high melting temperature. As an example of critical defect, detrimental crystallographic misalignments develop between dendrites in the casting of superalloy single-crystal turbine blades. Indeed, Blank *et al.*^[1] and Siredey *et al.*^[2] used Berg–Barrett topography to determine crystallographic disorientations between adjacent dendrites of turbine blade single crystals of Ni-based superalloys and showed that disorientations may attain several tenths of a degree. However, the origin of these disorientations cannot be readily determined from postmortem analysis. Such small disorientations and low-angle grain boundaries are known to build up while the morphological instability of the

solid-liquid interface is evolving into a cellular/dendritic array and solute microsegregation is increasing. This has motivated theoretical studies on the influence of elastic stress on pattern-forming instabilities in crystal growth. Directional solidification under uniaxial stress was considered by Cantat *et al.*,^[3] who analyzed the coupling between Asaro–Tiller–Grinfeld and morphological Mullins–Sekerka instabilities. This study shows that the critical velocity for the planar interface destabilization is lowered by the applied stress, which leads to a finer microstructure. Spencer *et al.*^[4] performed a linear stability analysis to study the morphological instability of strained alloy film growth. They predict an instability asymmetry between tension and compression as well as the critical wavelength and of instability in SiGe films. Such studies are limited, particularly because of the difficulty of establishing benchmark comparisons with experimental data.

From an experimental point of view, the most efficient way to directly observe the solid-liquid interface during the solidification of metallic alloys is the use of X-ray imaging techniques. Early visualization of the solid-liquid interface were based on radiography using laboratory sources, *e.g.*, to study solute redistribution and boundary layer propagation.^[5,6] The available brightness of the X-ray sources and geometrical resolution (up to 50 μm) were, however, not appropriate to observe the microstructure development. Later, microfocus X-ray sources producing increased incident photon flux were used by Koster, who investigated fluid flow in molten Ga and the global solidification microstructures in Ga-In,^[7] and by Kaukler *et al.*, to study the formation

G. REINHART and H. JUNG, Postdoctors, H. NGUYEN-THI and N. BERGEON, Assisting Professors, B. BILLIA, Senior Scientist, and N. MANGELINCK-NOËL, Researcher, are with L2MP, UMR 6137, Université Paul Cézanne – Aix-Marseille III, Campus Saint-Jérôme, 13397 Marseille Cedex 20, France. Contact e-mail: reinhart@l2mp.fr A. BUFFET, Postdoctoral Student, J. HÄRTWIG, Beamline Scientist, and J. BARUCHEL, Beamline Responsible, are with ESRF, BP 220, 38043 Grenoble, France. T. SCHENK, Researcher, is with the Laboratoire de Physique des Matériaux, Ecole des Mines de Nancy, Parc de Saurupt, 54042 Nancy Cedex, France.

Manuscript submitted May 30, 2007.

Article published online February 8, 2008

and engulfment of lead droplets in Al-Pb alloys.^[8] It is only in recent years that the high brilliance of the third generation synchrotron radiation was taken advantage of to carry out *in-situ* and real-time observations of microstructure formation by radiography on different alloy systems with satisfying spatial and time resolutions.^[9–12] In the field of solidification processing of materials, the dynamics of a series of phenomena, such as columnar-to-equiaxed transition (CET) in refined Al-Ni alloys,^[13] or fragmentation of dendritic crystals during columnar growth of Al-Cu alloys^[14] could be analyzed for the first time.

Synchrotron X-ray radiography imaging enables the investigation of the evolution of the microstructure morphology and of solute segregation. However, this technique gives no information on strains or disorientations in the growing solid. In order to have access to strains and defects during solidification, X-ray topography (XRT), based on the observation of diffracted beams, has to be used.^[15] First experiments were performed by Chikawa *et al.*, who used this technique with laboratory sources.^[16,17] These authors studied microdefects formation occurring during the melting and growth processes of metals and silicon, and showed that a possible origin of swirl defects in bulk crystals is the formation of droplets near the growth interface during remelting periods. Later, *in-situ* studies of solidification were performed with second generation synchrotron sources using synchrotron white beam X-ray topography (SWBXRT). The very intense X-ray beam provided by synchrotron sources allowed reduced exposure times, down to a few seconds (from several minutes) with laboratory sources. Besides observing the growth morphology, the specific benefit of using SWBXRT is the possibility of following the creation and evolution of crystal imperfection all along solidification. Interest is enhanced by the fact that several topographs displaying complementary information are captured simultaneously. Grange *et al.* carried out the first *in-situ* and real-time study of melting-solidification processes of an aluminum crystal with white synchrotron radiation.^[18] They observed that subgrain boundaries yield a diffuse zone of defects generated by the spreading out of the dislocations and confirmed that the perfection of the crystal decreases with increasing rate of crystallization. Matsumiya *et al.* followed solidification of 3 wt pct silicon steel alloy by synchrotron X-ray topography.^[19] They compared *in-situ* and postmortem cell spacing and found that they were of the same order. A more accurate study of cellular spacing was performed for Al-Cu alloys by Grange *et al.*, assuming that the topographs do not display large distortions of the microstructure morphology.^[20] The comparison of the measurements with available data on the same alloy brought out the influence of convection in the melt on the primary spacing and tip radius and on the cell-dendrite transition. Regarding the development of stresses and strains generated by microstructure formation, Grange *et al.* evidenced strain contrast preceding visible interface corrugation during the horizontal solidification of Al-Cu alloys.^[21] This contrast was attributed to the selective enhancement of fluctuations at the

solid-liquid interface when approaching the onset of morphological instability. Furthermore, these authors noticed that the cell bodies were always strained because of the nonuniform composition field in the solid associated to the cell shape. Billia *et al.*^[22] subsequently reported cell disorientation phenomena driven by the mechanical stresses applied on the growing solid by the cumulative torques and bending moments, which were concomitantly building up with the cellular microstructure.

Recently, a unique experimental setup, which allows the combination of synchrotron X-ray radiography (SXRR) and SWBXRT, has been implemented at the ID19 imaging beamline of the European Synchrotron Radiation Facility (ESRF, Grenoble, France). Initial observations were made during preliminary experiments for two Al-based alloys^[23] (Al-3.5 wt pct Ni and β -Al₃Mg₂). The aim of this article is to present a thorough analysis of experiments performed with this new setup on Al-3.5 wt pct Ni binary alloys. The preparation of the initial state before solidification, the formation dynamics of the nonplanar pattern at the solid-liquid interface, and the development of strains and microstructure defects during microstructure growth are analyzed. This study relies on the complementary information simultaneously provided by the association of synchrotron X-ray radiography and white beam topography.

II. EXPERIMENTS

The experiments were carried out at the ID19 beamline of ESRF. The alloy samples were solidified/melted vertically inside a Bridgman furnace (European Synchrotron Radiation Facility, Grenoble Cedex, France) described in References 23 and 24.

The furnace is made of two graphite heaters inserted in a boron nitride matrix that are independently adjusted to impose the desired longitudinal temperature gradient G on the sample. It is enclosed inside an ultra-high-vacuum (UHV) chamber at a pressure of 10^{-9} Torr at room temperature. Thin Al-3.5 wt pct Ni samples (37 mm \times 6 mm \times 0.2 mm) are adjusted into soft graphite crucibles designed to somewhat accommodate the thermal expansion stresses in the region surrounding of the solid-liquid interface. Each crucible is mounted in a holder connected to a motorized translation device. Sample solidification is achieved by pulling down the sample at a constant velocity (V) from the upper (hot) part of the furnace to the bottom (cold) part, whereas the applied temperature gradient (G) remains constant. The main surface of the sample (37 \times 6 mm²) is set perpendicular to the incident synchrotron X-ray white beam. The imaging setup offers the possibility of using two complementary X-ray imaging techniques for *in-situ* and real-time observation during the growth process: radiography and topography (Figure 1).

The transmitted beam is used for radiography. After crossing the sample, the X-ray beam is made monochromatic by a double Si(111) monochromator, at the energy of $E = 13.5$ keV in the present case. Radiographs are recorded using an ESRF FreLoN camera (Charge-coupled device-based camera, field of view

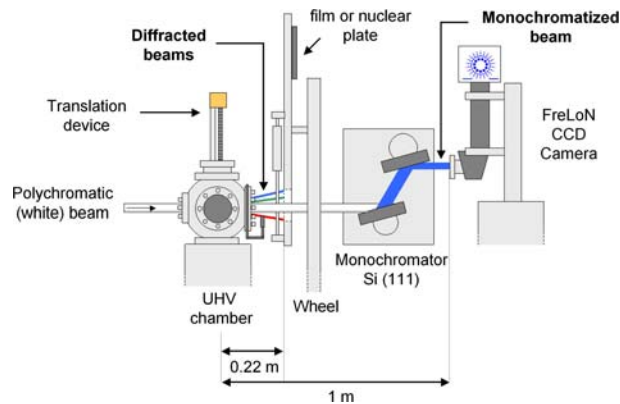


Fig. 1—Schematic drawing of the experimental setup developed at ID19-ESRF to perform combined synchrotron white beam X-ray topography and X-ray radiography during solidification of metals.

15 mm × 15 mm, pixel size 7.46 μm, European Synchrotron Radiation Facility, Grenoble Cedex, France) positioned 1 m after the furnace because of the space occupancy constraints imposed by the topography wheel (as subsequently discussed) and the Si monochromator. The radiograph contrast is basically caused by X-ray absorption, which is proportional to the atomic number and concentration of the alloy components. The SXRR images are *in-situ* and real-time undistorted pictures of the solidification microstructure. They give us direct

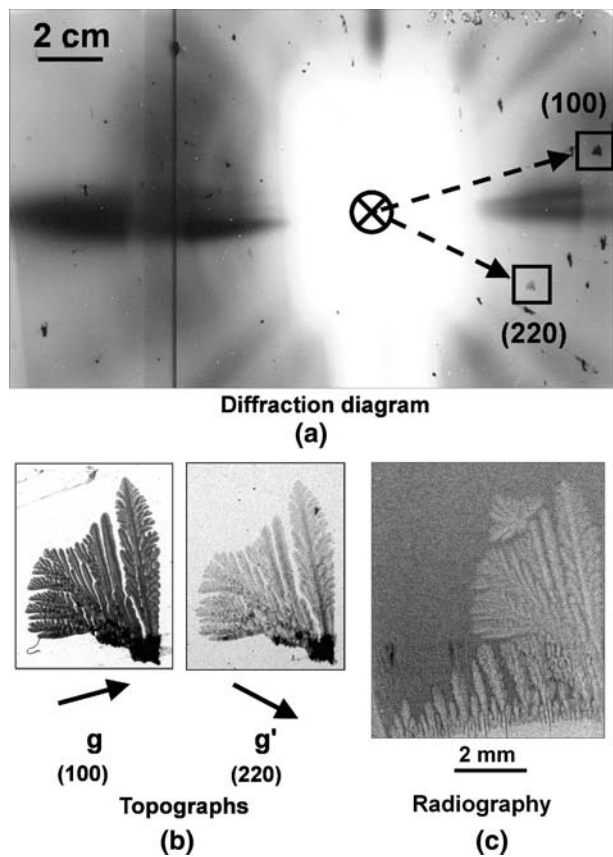


Fig. 2—Examples of the (a) diffraction diagram, (b) topographs, and (c) radiography recorded with the experimental device during solidification of an Al-3.5 wt pct Ni alloy.

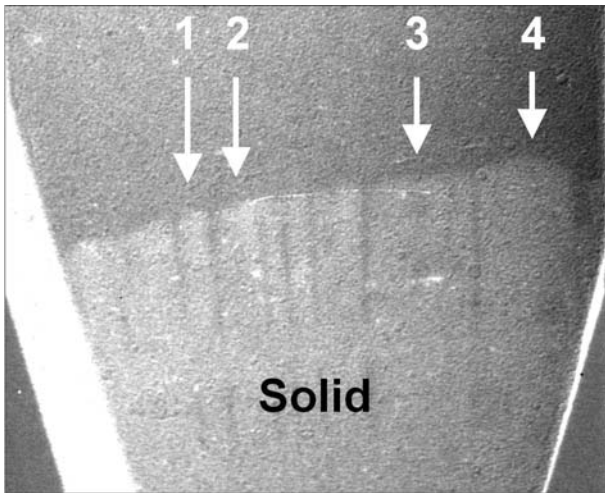
information on the morphology and the dynamics of the growing interface (Figure 2(c)). SWBXR makes use of the beams diffracted by the solidified alloy.

In practice, Laue diagrams (Figure 2(a)) are discontinuously recorded on either high-resolution films (spatial resolution 5 μm) or nuclear plates (spatial resolution 1 μm) stored on a wheel placed after the UHV chamber. This wheel has an empty window to let the direct X-ray beam pass through for radiography, and seven housings for the high-resolution films or nuclear plates. It is monitored by a computer installed in the control room of the ID19 beamline, next to the experimental room, so that a series of exposures can be performed at will without interrupting the illumination of the sample. Because of the size of the UHV chamber, the distance between the sample and the wheel is 22 cm, which is large compared with what is commonly used (a few centimeters). This distance limits the number of diffracted beams that impinge on the film/plate. Each spot in the Laue diagram is actually a topograph of some tiny or large part of the solid (grain, dendrite, dendrite arm, etc.). Each topograph is identified by its diffraction vector \mathbf{g} and Miller indices (Figure 2(b)). In favorable cases, when enough images of the same solid part can be identified in the Laue diagram, indexation is automatically performed with the OrientExpress software (Laboratoire des matériaux et du génie physique, Grenoble, France). When the recorded spots are too few, indexation is manually performed using stereographic projections and angle tables, in particular, using additional information on dendrite orientation gained from radiography. Very small disorientations between grains and in the solidification microstructure (some tenths of a degree) can thus be precisely measured. The interpretation of the contrasts in topographs using the dynamical theory of diffraction is feasible only for crystals of very high quality (*i.e.*, with a density of defects less than 10 cm/cm³). At higher densities of defects or under strain, such as in our experiments, the pictures become rapidly and strongly distorted with even significant asterism. Then, the topograph contrasts are generally too complex to go beyond qualitative interpretation.

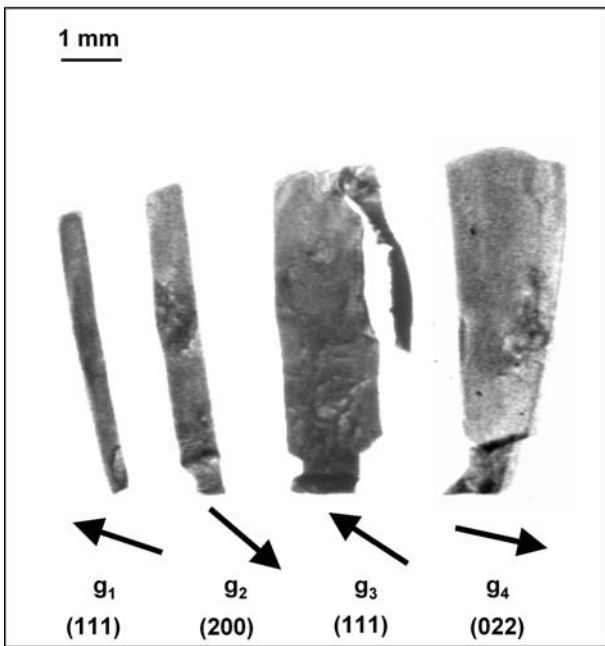
III. RESULTS AND DISCUSSION

A. Initial State before Solidification

The experimental protocol to obtain the initial solid-liquid interface is identical for all samples. This step is observed by SXRR. The lower part of the Al-3.5 wt pct Ni sample is placed in the field of view of the FReLoN camera. A thermal gradient $G = 30$ K/cm is applied by adjusting the temperature of heaters and the sample is partially melted by gradually increasing these temperatures in order to position the solid-liquid interface at the bottom of the field of view. This is followed by a thermal stabilization period. Figure 3(a) shows a radiograph of the solid-liquid interface after 5 hours of stabilization. The liquid phase is richer in solute (nickel) than the solid phase, and appears in dark gray. The curvature of the solid-liquid interface is caused by a residual transverse temperature gradient in the sample. The solid phase is



1 mm
(a)



(b)

Fig. 3—(a) Radiography of the solid-liquid interface and (b) topographs of 4 aluminum grains after 5 h of stabilization in an applied temperature gradient of $G = 30$ K/cm. Aluminum solid grains formed during the stabilization phase are surrounded by solute-rich liquid and are of good crystalline quality.

composed of several aluminum grains separated by Ni-rich liquid channels, more or less wide. This grain morphology is caused by the temperature gradient zone melting (TGZM) mechanism that occurs during the stabilization phase. This mechanism, introduced by Pfann,^[25] was thoroughly described for cylindrical rods of Al-1.5 wt pct Ni alloys by Nguyen Thi *et al.*,^[26] who performed stabilization experiments and postmortem analyses. Before melting, the alloy sample is composed of equiaxed grains of primary aluminum phase surrounded by eutectic (Al + Al₃Ni), and containing eutectic inclusions a few micrometers in size. Thus, a

mushy zone forms during the melting phase because of the multiphase nature of the starting material: when the solid reaches the eutectic temperature $T_E = 913$ K, the eutectic phase melts prior to aluminum and gives way to liquid channels and droplets with eutectic composition $C_E = 5.7$ wt pct Ni. Most of these liquid elements migrate toward higher temperatures under the effect of the vertical thermal gradient, until they reach the solid-liquid interface. Under this migration, the mushy zone is progressively cleared of liquid and the melt above is enriched in solute. The TGZM process, together with high-temperature grain ripening, eventually results in a few large aluminum grains separated by vertical liquid channels. These grains have different crystallographic orientation and each one generates its own diffraction diagram, which is recorded during the exposure of a high-resolution film. Figure 3(b) shows a picture of the most intense diffraction spot obtained for 4 grains. The shape of each grain is easily recognizable and the gray contrasts are rather light and uniform. We can conclude from these observations that the initial solid aluminum grains formed during the stabilization phase are of good crystalline quality and only slightly strained.

B. Observation of the Initial Solidification Transient

In the first stage of solidification, disturbances caused by Mullins–Sekerka instability^[27] appear at the solid-liquid interface and cells or dendrites develop, as illustrated in Figure 4. Figures 4(a) and (b) are two pictures of the solid-liquid interface recorded after 30 minutes of pulling at a velocity of $V = 1$ μ m/s. They show the development of a cellular pattern without and with image processing, respectively. The image processing consists in subtracting the pictures of the initial state just before applying the pulling rate from the current pictures, which contain the solidification microstructure. This removes the artifacts in the images because of dust or defects on the crucible wall, as well as variation of the incident X-ray beam intensity or sample thickness. After image processing, the initial solid appears in dark gray in the bottom of the picture (Figure 4(b)), whereas the microstructure solidified in pulling appears brighter and with a sharper contrast than on the raw radiographic pictures (Figure 4(a)). Solute rejected during solidification accumulates in the left part of the sample because of the initial interface asymmetry and fluid flow driven by the horizontal temperature gradient. Consequently, the transition from interface corrugation to cells is slower on the left than on the right. The shallow cell morphology is much more visible on topographs (Figure 4(c)) because the spatial resolution is better and the liquid is not imaged. An average cellular wavelength of $\lambda_1 = 300$ μ m can be determined. Then, sidebranches begin to form on the largest cells (grain 4), which indicates the inception of dendrite growth. Equal-thickness fringes are visible within the solid as in the (111)-reflection of grain 3. This observation points out the high crystalline quality of the solid microstructure in its early stage of growth when it is surrounded by alloy melt. This is in agreement with previous studies on the onset of the morphological instability performed during horizontal

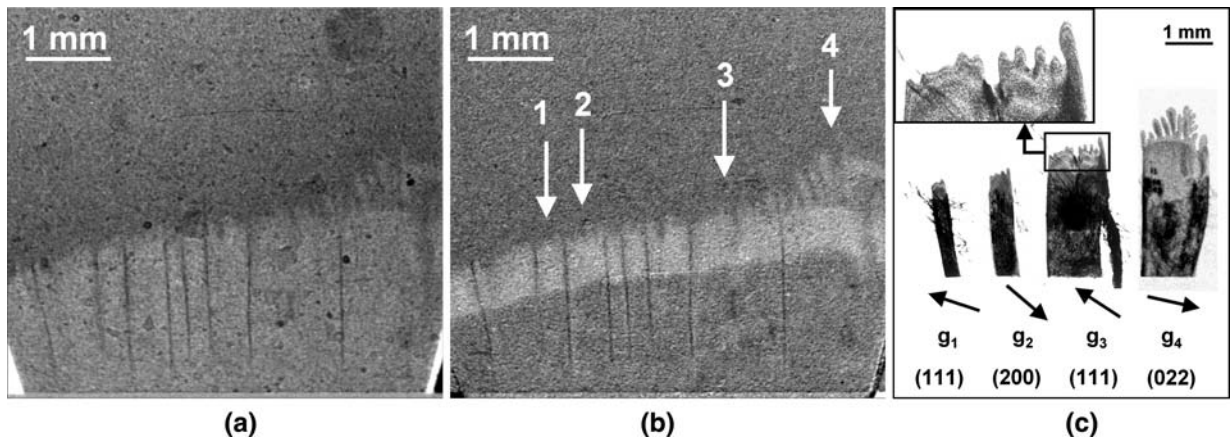


Fig. 4—Radiography of the solid-liquid interface (a) without and (b) with image processing and (c) topographs of 4 aluminum grains after 30 min of pulling at $V = 1 \mu\text{m/s}$ in an applied temperature gradient $G = 30 \text{ K/cm}$. The interface is undergoing morphological instability and a cellular pattern is developing. Equal thickness fringes visible on topographs point out that the solidifying crystals are of high crystalline quality. Strong black contrasts at the bottom part of the topographs reveal the occurrence of stresses when the remaining liquid in contact with the crucible wall has solidified.

solidification of Al-Cu alloys by Grange *et al.* using synchrotron X-ray topography.^[20] Yet, aluminum grains become highly stressed when the remaining liquid in contact with the crucible wall solidifies, forming a eutectic phase, as shown by the strong black contrasts at the bottom of each topograph in Figure 4(c). The strain induced by the eutectic entrapment will be further described later. In the subsequent stage (Figure 5(a)), the eutectic front appears on the left because of local increase of solute concentration in the liquid. Amplitude and lateral size of dendrites on the right increase concomitantly causing a strong screening of the growth of the neighboring cells. The general shape of the microstructure is then composed of a few dendrites localized on the right and markedly protruding into the liquid phase with a eutectic front at their bases. A steady state is finally reached when the dendrites and the eutectic front jointly propagate at a constant velocity.

C. Formation of Microstructural Defects during Dendrite Growth

The synchrotron X-ray topography technique is the method of choice to access to microstructure disorientations because it is based on diffraction. Any small change in cell or dendrite orientation with respect to the incident X-ray beam generates a displacement of its Laue images. Furthermore, when the interface microstructure is cumulating disorientation its Laue images may break into several pieces with time, making analysis intricate. In fact, clearer insight is obtained from combined synchrotron X-ray radiography and topography (Figure 5). As an example, Figure 5(b) is a topography of the two dendrites coming from aluminum grain 4 shown in Figure 5(a). One can see that the Laue images of a secondary arm of the left dendrite, noted I, and a portion of the primary trunk of the right dendrite, noted II, are shifted from the main image, whereas the structure remains fully connected in radiography. This

observation means that the crystallographic orientation of those two parts has changed during growth.

Several disorientations occurred all along the development of the dendrites and were followed *in situ* and real time with our current experimental device. Some are irreversible, as the disorientation of the secondary arm I on the left of Figure 5(b) that still appears at the same position 10 minutes later (Figure 5(d)). In this last topography, the arm appears to be more developed because of its growth and strained because of its entrapment in the eutectic phase. Other disorientations are reversible, for instance, the image II of the portion of primary trunk on the right of Figure 5(b) reappears at its initial location on the topograph Figure 5(d), leaving behind an empty space in II. By analyzing the displacement of Laue images on different diffraction spots, we have been able to establish that the portion of primary trunk achieved a rotation of some tenth of degrees around its growth axis. This rotation can be interpreted as an elastic mechanism resulting from the action of the torque induced by shear stress that builds up with the growth shape, as previously suggested by Billia *et al.*^[22]

Another disorientation mechanism is highlighted by the analysis of the displacement of the secondary arm encircled in dashed line on the topographs in Figure 6(b). We have been able to establish from topographs that the entire arm rotated by 3 deg around the incident direct beam axis and 0.3 deg around the y -axis perpendicular to the incident direct beam. The rotation around the incident beam axis is obvious on radiographs (Figure 6(a)), which are actually projections of the structure along the incident beam. This phenomenon rapidly occurs (less than 1 second), and the successive rotation of each secondary arms is usually observed during the growth of dendritic microstructures. The origin of this disorientation is the bending mechanism described by Billia *et al.*^[22] In our case, horizontal secondary arms generate an extrinsic mechanical bending moment caused by earth gravity.

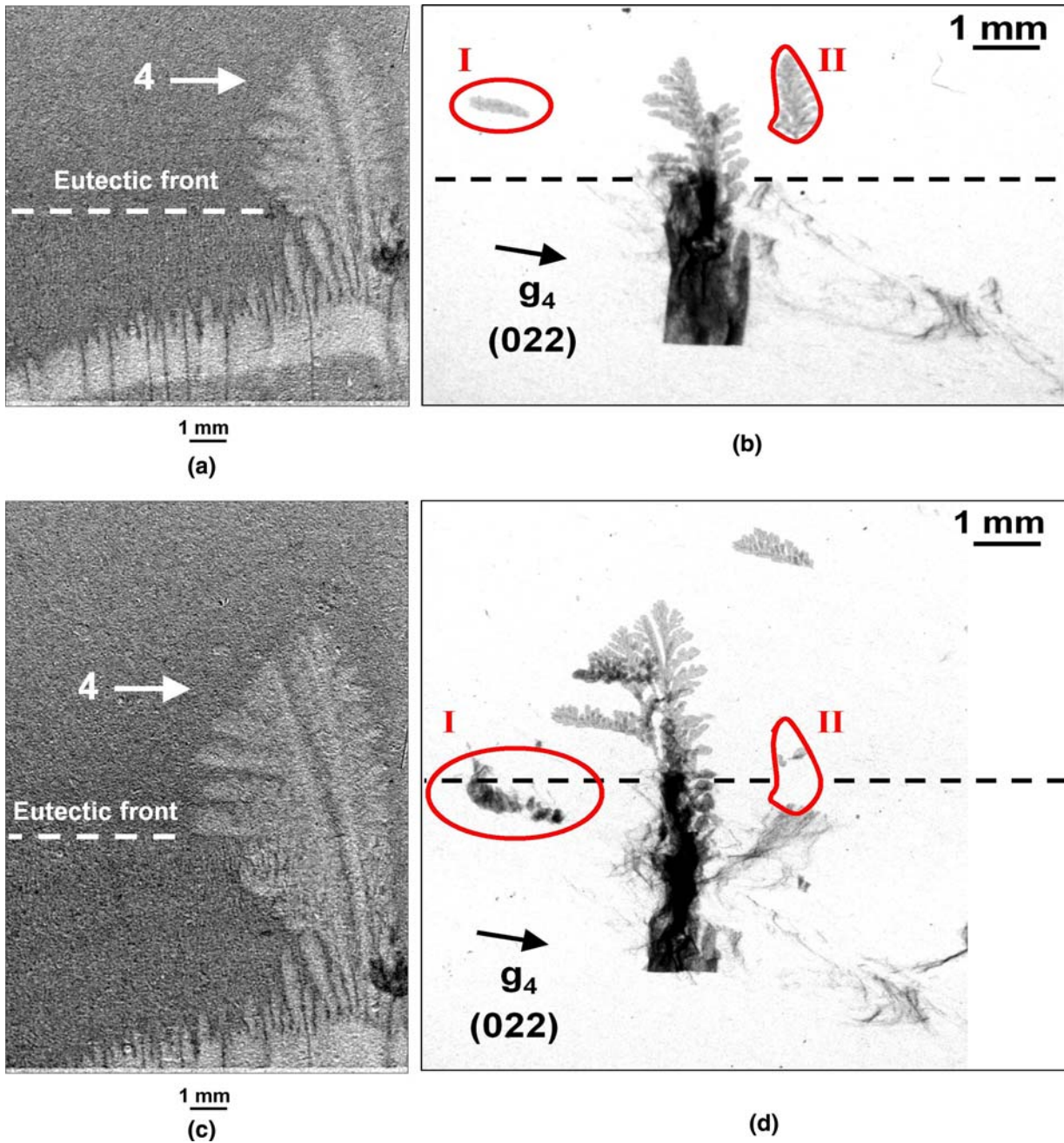


Fig. 5—(a) and (c) Radiographs of the solid-liquid interface and (b) and (d) topographs of aluminum grains 4 after 45 and 55 min of pulling, respectively, at $V = 1 \mu\text{m/s}$ in an applied temperature gradient $G = 30 \text{ K/cm}$. (b) The disorientation of a secondary arm and of a portion of the primary trunk provoked the displacement of their image in topography. The image of the previously disoriented primary trunk reappears at its initial position in (d).

Because of the lower moment of inertia there, stresses are localized at the thin solid necks that attach the arms to the primary trunk, and cumulate as the arms grow and become heavier (Figure 7(a)). After a certain time, the yield stress is exceeded at the necks, which causes their sudden and irreversible rotation, carrying the entire single crystal along with it (Figure 7(b)). An estimation of the bending stress σ_B at the neck can be analytically performed by considering secondary arms as parallelepipeds connected to the primary trunk by a thin cylindrical neck (Figure 7(b)). The bending

moment, M_B , moment of inertia for neck bending, I_B , and bending stress, σ_B , at the neck, can be written by using the principle of calculation proposed by Billia *et al.*:^[22]

$$M_B = (\rho_S - \rho_L) \cdot V \cdot g \cdot L/2 \quad [1]$$

$$I_B = \pi \cdot r^4/4 \quad [2]$$

$$\sigma_B = M_B \cdot r/I_B \quad [3]$$

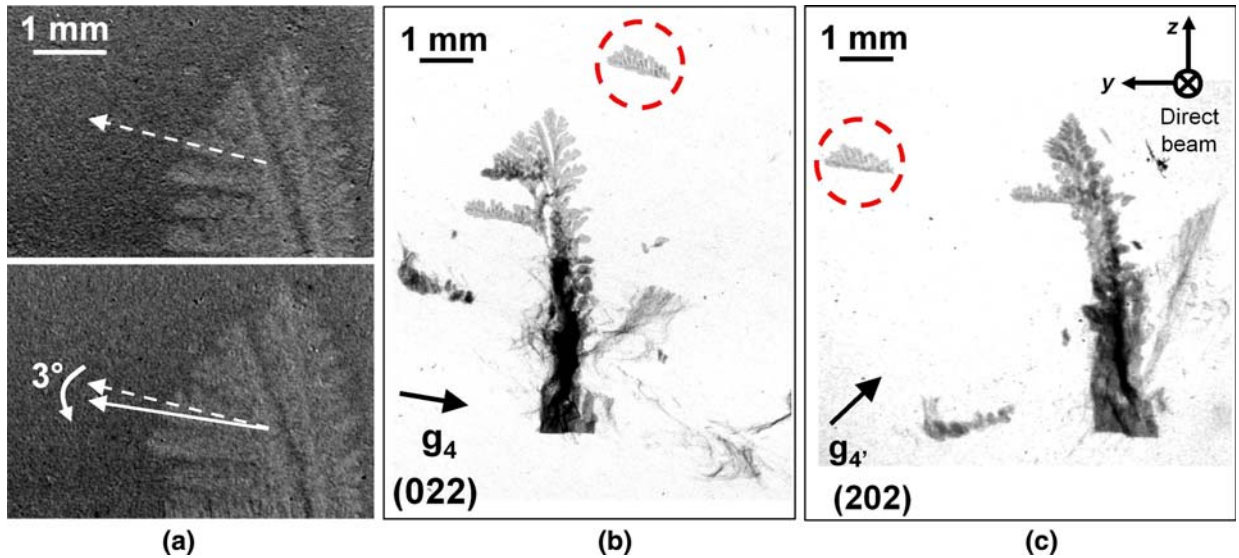


Fig. 6—(a) Radiographs of the solid-liquid interface recorded after 55 and 58 min and (b) and (c) topographs recorded in the same exposure after 57 min of pulling at $V = 1 \mu\text{m/s}$ in an applied temperature gradient $G = 30 \text{ K/cm}$. Radiographs show the bending of a secondary arm, which rotated by 3 deg around the incident direct beam axis. The measure of the displacement of the secondary arm image on topographs indicates a rotation of 3 deg around the incident direct beam axis and also of 0.3 deg around the y -axis.

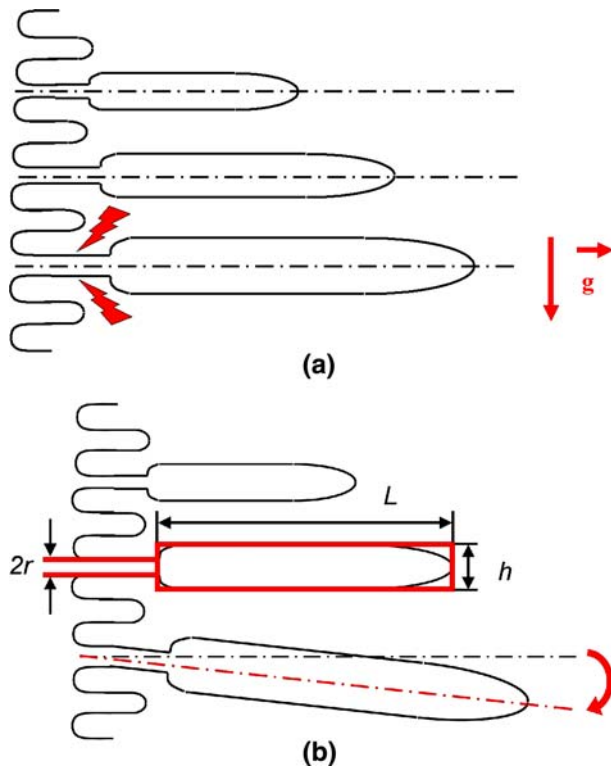


Fig. 7—Schematic representation of the bending of a secondary arm. (a) Stresses are localized and cumulate at the thin solid necks, which attach the arm to the primary trunk. (b) The arm rotates when the yield stress is exceeded at the neck.

where ρ_S and ρ_L are the liquid and solid densities, V the volume of solid aluminum, g the gravity acceleration, L the length of the full arm length, and r the radius of the neck (Figure 7(b)). We measured the rotation that occurred when the arms reach at an average length of

$1500 \mu\text{m}$ and height of $375 \mu\text{m}$. We assume that the thickness of the arms is $e = 200 \mu\text{m}$ (thickness of sample) and a solid fraction $f_s = 0.7$. By using $\rho_S - \rho_L = 80 \text{ kg/m}^3$ and taking $6 \mu\text{m} < r < 15 \mu\text{m}$, the minimum and maximum values of neck radius measured on topographs, we find that $0.02 \text{ MPa} < \sigma_B < 0.27 \text{ MPa}$. The large difference between the two values is because of the variation in r^4 of the moment of inertia, which has a strong effect on the value of σ_B . Nevertheless, this estimation gives us an order of magnitude for the elastic limit of aluminum near the melting point. The maximum value is of the same order as the yield stress at the melting point of 0.6 MPa used by Pilling and Hellawell,^[28] by reducing by an order of magnitude the value extrapolated from low temperature data, or the value of 0.13 MPa obtained by Billia *et al.*^[22] for the bending of cells during horizontal solidification of Al-Cu alloys. Our estimation shows that the low stress caused by gravity is sufficient to provoke disorientations of several degrees of parts of dendritic microstructures, and can, therefore, induce the growth of adjacent dendrites with different crystallographic orientation. This would eventually lead to misalignments between dendrites comparable with those observed after growth on real superalloy blades.^[1,2]

According to deformation mechanism maps^[29] for pure aluminum, the transition from an elastic to a plastic diffusional creep deformation regime, or Nabarro–Herring creep, can occur for some tenths of MPa near the melting point. This transition can be at the origin of the bending phenomenon because the critical stress previously estimated is of the same order of magnitude. Furthermore, Nabarro–Herring creep is caused by the diffusional flow of single atoms by bulk transport, and deformations rapidly propagate in this regime. This behavior could explain that the bending of secondary arms occurs in less than 1 second, as soon as

the yield stress is reached. Further investigations will be performed in order to ascertain this assumption and to obtain a more precise estimation of the yield stress. Numerical methods can be used to model stresses and strains during growth as recently performed by Yang *et al.*,^[30] who used a finite element model to calculate stress and strain fields in moderate agitated fluid. The development of a numerical code to estimate strains and stresses during the development of structures with a complex dendritic morphology has yet to be done.

D. Formation of Strains Following the Solidification of Eutectic Phase

Figure 8(a) shows a radiograph of the solid-liquid interface after 45 minutes of growth and a topograph of the primary aluminum grain 1. Black contrasts appear at the bottom of the topograph, where the temperature is below the eutectic temperature, T_E . As previously mentioned, aluminum grains become highly stressed when the remaining liquid solidifies forming a eutectic

phase (Figure 4(c)). At the beginning of the experiment, aluminum grains are surrounded by liquid; the microstructures thus develop without external stress and their morphology is easily recognizable in topographs. The eutectic front appears above the slower aluminum cells, as illustrated in the radiographs in Figures 8(b) and (c). For the investigated alloy, the eutectic phase is composed of α -Al and β -Al₃Ni lamellae. Eutectic lamellae cannot be resolved in radiography, but the topographs in Figures 8(b) and (c) reveal that α -Al lamellae are imaged and grow with a common crystallographic orientation with the previous aluminum microstructure. This can be explained by taking into account that the eutectic phase nucleates from the solute-rich liquid on already present α -Al aluminum grains, and α -Al lamellae, therefore, retain the crystallographic orientation. However, these lamellae are strongly strained in the course of growth and only appear as tousled trails.

The distortions observed for the α -Al lamellae and the primary aluminum structures following the solidification of the eutectic phase can be attributed to several

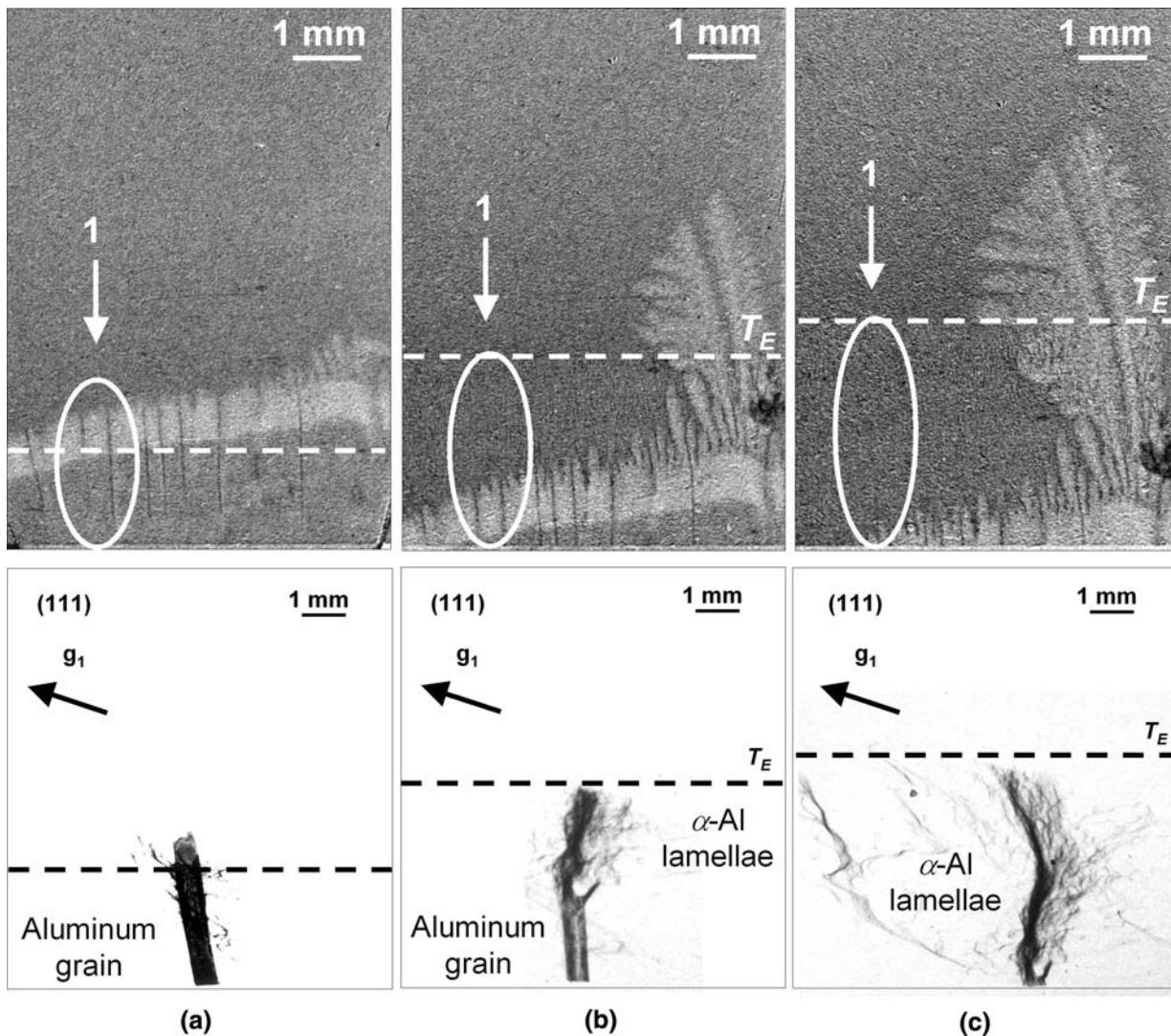


Fig. 8—Sequence of radiographs of the solid-liquid interface and topographs of grain 1 showing the entrapment of aluminum grains in the eutectic phase. The strained growth of α -Al lamellae forms tousled trails on topographs.

phenomena. The Al-Al₃Ni system is a well-known metal matrix composite (MMC) where aluminum is the matrix and the intermetallic compound Al₃Ni act as reinforcement material. The reinforcement material is usually harder and has better mechanical properties than the matrix. When a composite is subjected to temperature changes, thermal stresses are generated because of the mismatch in thermal expansions between the matrix and the reinforcement material, significantly influencing its mechanical properties.^[31,32,33] In our case, the distortion of α -Al lamellae can be caused by such thermal stresses because α -Al lamellae have a higher thermal expansion coefficient than the β -Al₃Ni lamellae ($\alpha_{Al} = 25 \cdot 10^{-6} \text{ K}^{-1}$ and $\alpha_{Al_3Ni} = 16 \cdot 10^{-6} \text{ K}^{-1}$).^[34] Similarly, the eutectic phase has a lower thermal expansion coefficient than the primary aluminum microstructure. The eutectic phase, which solidifies around the primary aluminum grains, can, therefore, induce tensile stresses in the dendritic microstructure and be the origin of the strong black contrasts previously mentioned. Last, when the eutectic phase solidifies from the remaining liquid, the solid fills the entire space within the crucible. The contact of the solid with the inner wall can induce stresses in the eutectic phase, which are then transmitted to the aluminum microstructure. We observed that the graphite foils we used as soft crucible are stuck to the sample at the end of the experiments. This suggests that the crucible also exerts a tensile stress on the solid phase following the shrinkage because of solidification.

When the steady state is reached, the formation of multiple microstructure defects, such as arms and portions of trunk disorientations, lead to the formation of very fragmented images in topographs (Figure 9(b)). Strong black contrasts following the eutectic formation strongly deteriorate the legibility of the images. The microstructure is then very difficult to recognize in topographs compared with radiographs (Figure 9). Almost all secondary arms are disoriented, and only

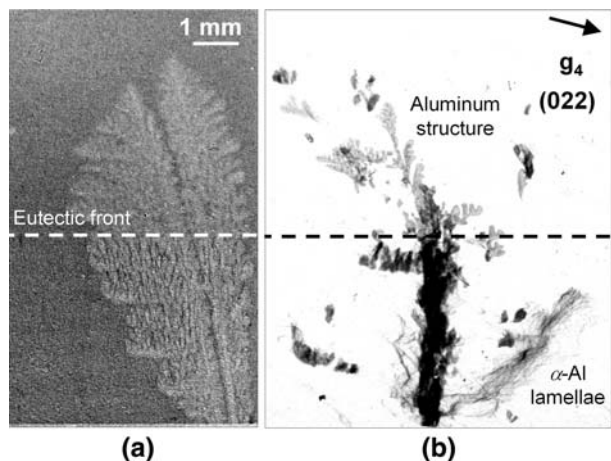


Fig. 9—(a) Radiography of the solid-liquid interface and (b) topography of the dendritic grain after 1 h and 17 min of pulling at $V = 1 \mu\text{m/s}$ in an applied temperature gradient of $G = 30 \text{ K/cm}$. The dendritic microstructure is hardly recognizable on the topograph because of the successive defects formation during the growth process and stresses following the entrapment in the eutectic phase.

the distorted images of the primary trunk and α -Al eutectic lamellae remain.

IV. CONCLUSIONS

We studied the directional solidification of Al-3.5 wt pct Ni binary alloys using a unique experimental setup developed at ID19-ESRF to perform combined synchrotron white beam X-ray topography and X-ray radiography during solidification of metallic alloys. The different steps of a directional solidification process were characterized.

1. The initial state before solidification is composed of several aluminum grains surrounded by solute-rich liquid channels that formed during the thermal stabilization phase by TGZM mechanism. Grains have different crystallographic orientations and are of good crystalline quality.
2. Cellular then dendritic patterns develop during the initial solidification transient. The solidifying crystals are of high crystalline quality at their early stage of growth. A steady state is reached with some dendrites markedly protruding into the liquid phase propagating with a eutectic front at their bases.
3. During dendrite growth, several disorientations of secondary arms and even of portions of primary trunks are observed and were quantified. The origin of the disorientations is the accumulation of mechanical constraints induced by shear stress and earth gravity.
4. Microstructures are immediately strained after their entrapment in the eutectic phase, which solidifies from the remaining liquid in contact with the inner wall. α -Al eutectic lamellae grow with the same crystallographic orientation as the microstructure and appear as tousled trails in topography.

These observations clearly point out that the dendritic microstructures, as well as those in the eutectic phase, are undergoing several mechanical constraints during their growth. Complementary works at the ESRF are planned in order to improve the understanding of these phenomena.

ACKNOWLEDGMENTS

The authors thank Gerd-Ulrich Grün, Hydro Aluminium GmbH (Deutschland), for providing the samples used in the series of experiments presented in this article and the ESRF ID19 staff members for their scientific and technical support before and during the experiments.

OPEN ACCESS

This article is distributed under the terms of the Creative Commons Attribution Noncommercial License which permits any noncommercial use, distribution, and reproduction in any medium, provided the original author(s) and source are credited.

REFERENCES

1. E. Blank, W. Kurz, and M. Rappaz: *Helvetica Physica Acta*, 1985, vol. 58, pp. 469–83.
2. N. Siredey, M. Boufoussi, S. Denis, and J. Lacaze: *J. Cryst. Growth*, 1993, vol. 13, pp. 132–46.
3. I. Cantat, K. Kassner, C. Misbah, and H. Müller-Krumbhaar: *Phys. Rev. E*, 1998, vol. 58, p. 6027.
4. B.J. Spencer, P.W. Voorhees, and J. Tersoff: *Phys. Rev. B*, 2001, vol. 64, p. 235318.
5. J. Forsten and H.M. Miekkoaja: *J. Inst. Met.*, 1971, vol. 99, p. 31.
6. M.P. Stephenson and J. Beech: *Proc. Int. Conf. on Solidification and Casting of Metals*, Sheffield, July 18–21, 1977, pp. 34–38.
7. J.N. Koster: *J. Mater.*, 1977, vol. 49, p. 31.
8. W.F. Kaukler, F. Rosenberg, and P.A. Curreri: *Metall. Mater. Trans. A*, 1977, vol. 28A, p. 1705.
9. R.H. Mathiesen, L. Arnberg, K. Ramsokar, T. Weitkamp, C. Rau, and A. Snigirev: *Metall. Mater. Trans. B*, 2002, vol. 33B, pp. 613–23.
10. H. Yasuda, I. Ohnaka, K. Kawasaki, A. Sugiyama, T. Ohmichi, J. Iwane, and K. Umetani: *J. Cryst. Growth*, 2004, vol. 262, pp. 645–52.
11. H. Nguyen Thi, J. Gastaldi, T. Schenk, G. Reinhart, N. Mangelinck-Noël, V. Cristiglio, B. Billia, B. Grushko, J. Härtwig, H. Klein, and J. Baruchel: *Phys. Rev. E: Status Phys.*, 2006, vol. 74, p. 031605.
12. B. Li, H.D. Brody, D.R. Black, H.E. Burdette, and C. Rau: *J. Phys. D: Appl. Phys.*, 2006, vol. 39, pp. 4450–56.
13. G. Reinhart, N. Mangelinck-Noel, H. Nguyen-Thi, T. Schenk, J. Gastaldi, B. Billia, P. Pino, J. Hartwig, and J. Baruchel: *Mater. Sci. Eng. A*, 2005, vols. 413–414, pp. 384–88.
14. R.H. Mathiesen, L. Arnberg, P. Bleuet, and A. Somogvi: *Metall. Mater. Trans. A*, 2006, vol. 37A, pp. 2515–24.
15. D.K. Bowen and B.K. Tanner: *High-Resolution X-Ray Diffraction Topography*, Taylor & Francis Ltd., Oxford, United Kingdom, 1998.
16. J. Chikawa: *J. Cryst. Growth*, 1974, vols. 24–25, p. 61.
17. J. Chikawa and S. Shirai: *J. Cryst. Growth*, 1977, vol. 39, pp. 328–40.
18. G. Grange, C. Jourdan, A.L. Coulet, and J. Gastaldi: *J. Cryst. Growth*, 1985, vol. 72, p. 784.
19. T. Matsumiya, W. Yamada, T. Ohashi, and O. Nittono: *Metall. Mater. Trans. A*, 1987, vol. 18A, p. 723.
20. G. Grange, J. Gastaldi, C. Jourdan, and B. Billia: *J. Cryst. Growth*, 1995, vol. 151, pp. 192–99.
21. G. Grange, C. Jourdan, J. Gastaldi, and B. Billia: *Acta Mater.*, 1997, vol. 45, pp. 2329–38.
22. B. Billia, N. Bergeon, H. Ngyuen Thi, H. Jamgotchian, J. Gastaldi, and G. Grange: *Phys. Rev. Lett.*, 2004, vol. 93, p. 126105.
23. A. Buffet, G. Reinhart, T. Schenk, H. Nguyen-Thi, J. Gastaldi, N. Mangelinck-Noël, H. Jung, J. Härtwig, J. Baruchel, and B. Billia: *Phys. Status Solidi A*, 2007, vol. 204, pp. 2721–27.
24. H. Nguyen Thi, H. Jamgotchian, J. Gastaldi, J. Härtwig, T. Schenk, H. Klein, B. Billia, J. Baruchel, and Y. Dabo: *J. Phys. D: Appl. Phys.*, 2003, vol. 36, pp. A83–A86.
25. W.R. Pfann: *Trans. AIME*, 1955, vol. 203, p. 961.
26. H. Nguyen Thi, B. Drevet, J.M. Debierre, D. Camel, Y. Dabo, and B. Billia: *J. Cryst. Growth*, 2003, vol. 253, pp. 539–48.
27. W.W. Mullins and R.F. Sekerka: *J. Appl. Phys.*, 1964, vol. 35, p. 444.
28. J. Pilling and A. Hellawell: *Metall. Mater. Trans. A*, 1996, vol. 27, p. 229.
29. M.F. Ashby: *Acta Metall.*, 1972, vol. 20, pp. 887–97.
30. Z. Yang, C.G. Kang, and Z.Q. Hu: *Metall. Mater. Trans. A*, 2005, vol. 36A, pp. 2785–92.
31. D.A. Koss and S.M. Copley: *Metall. Trans.*, 1971, vol. 2, p. 1557.
32. K. Wakashima, T. Kawakubo, and S. Umekawa: *Metall. Trans. A*, 1975, vol. 6A, p. 1755.
33. K. Wakashima and S. Umekawa: *Metall. Trans. A*, 1976, vol. 7A, p. 1952.
34. G. Garmong: *Metall. Trans.*, 1974, vol. 5, pp. 2191–97.